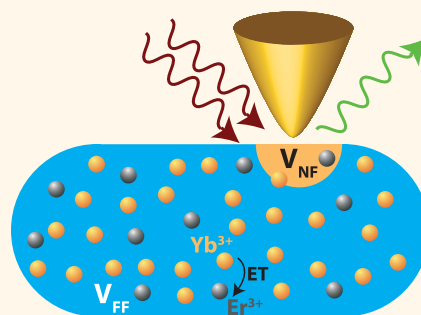# Tip Enhancement of Upconversion Photoluminescence from Rare Earth Ion Doped Nanocrystals

Nina Mauser,[†] Dawid Piatkowski,[‡] Tobia Mancabelli,[†] Marcin Nyk,[§] Sebastian Mackowski,[‡] and Achim Hartschuh*,[†]

[†]Department Chemie and CeNS, Ludwig-Maximilians-Universität München, 81377 München, Germany, [‡]Institute of Physics, Faculty of Physics, Astronomy and Informatics, Nicolaus Copernicus University, Grudziadzka 5, 87-100 Torun, Poland, and [§]Institute of Physical and Theoretical Chemistry, Wroclaw University of Technology, Wybrzeze Wyspianskiego 27, 50-370 Wroclaw, Poland

ABSTRACT We present tip-enhanced upconversion photoluminescence (PL) images of Er^{3+}- and Yb^{3+}-doped $NaYF_4$ nanocrystals on glass substrates with subdiffraction spatial resolution. Tip—sample distance dependent measurements clearly demonstrate the near-field origin of the image contrast. Time-resolved PL measurements show that the tip increases the spontaneous emission rate of the two emission channels of Er^{3+} in the visible region. Very efficient enhancement of upconversion PL is discussed in the context of the two-photon nature of the excitation process and homoenergy transfer between the ions within the nanocrystals. Comparison between different nanocrystals and tips shows a strong influence of the tip shape on the image contrast that becomes particularly relevant for the larger dimensions of the investigated nanocrystals.

Tip-enhanced near-field optical microscopy (TENOM) is a scanning probe technique that is widely employed to study nanostructures with subdiffraction spatial resolution combined with substantial signal enhancement.[1] It exploits the locally enhanced electric fields in the vicinity of a sharp metal tip to amplify the excitation and emission rates in a nearby sample object. In this sense the tip acts as an optical antenna[2] that can be used to enhance multiple optical responses, including Raman scattering, photoluminescence, electroluminescence, and photocurrent.[1] Because of the rapid decay of the locally enhanced field inside the sample material, on the order of 10 nm depending on the tip size,[3] TENOM is a surface-sensitive technique. It is hence ideally suited for the investigation of very thin nanomaterials or subsurface structures and has been applied to a huge variety of materials, including polymer thin films,[4] carbon nanotubes,[3,5,6] inorganic semiconducting nanowires,[7−9] single molecules,[10,11] RNA,[12] and graphene.[13,14]

In the simplest case the enhanced detected signal scales linearly with the incident laser intensity, while its source remains completely local. For higher excitation intensities nonlinear processes such as two-photon absorption[15] and stimulated Raman scattering[16] could become important, while for spatially extended structures energy transport[4,17] leading to nonlocal emission can complicate the image contrast formation.

Rare earth ion doped crystals provide an efficient conversion of near-infrared into visible light and are thus of particular interest for a variety of applications such as multimodal bioimaging contrast agents[18,19] and solar cell activators.[20] Metal particle enhanced upconversion has been reported by several groups to date. The first results were obtained by introducing silver particles into the crystal matrix.[21−23] More recent studies were based on depositing nanocrystals on a gold pyramid substrate[24] or on a gold nanograting.[25] Schietinger et al.[26] performed experiments in which they controlled the particle—nanocrystal distance using an AFM. The authors demonstrated
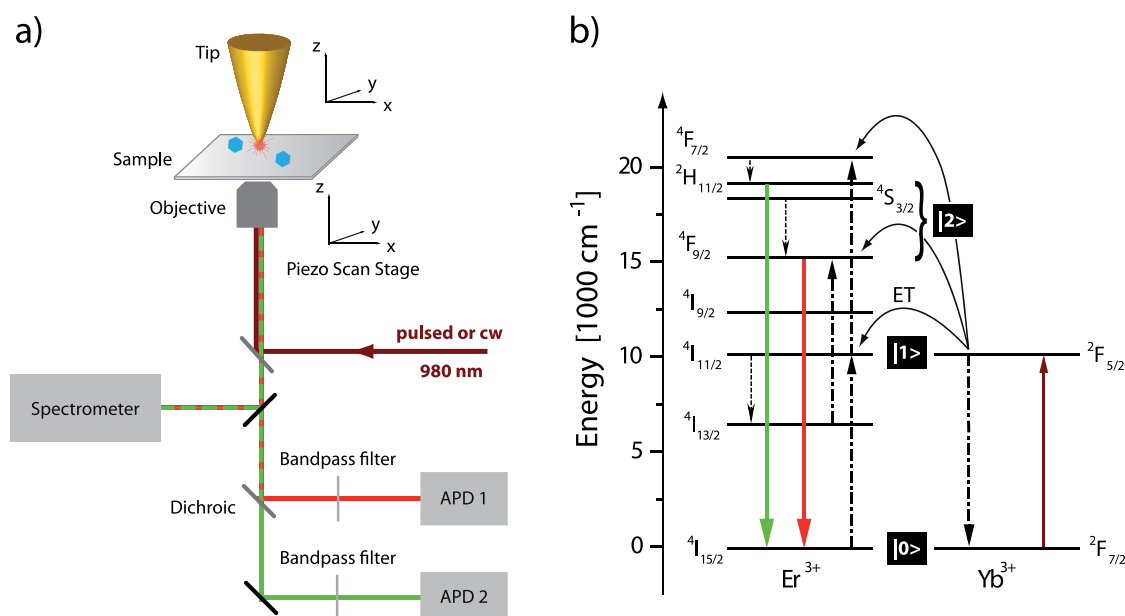
Figure 1. (a) Schematic of the experimental setup. An inverted confocal microscope was combined with a tuning fork AFM instrument to scan a gold tip in proximity of the sample surface. The detection path consisted of two channels equipped with avalanche photodiodes (APDs). Spectral bandpass filters centered at 550 ± 25 and 660 ± 15 nm were used to select the $^{4}S_{3/2}$, $^{2}H_{11/2} \rightarrow {}^{4}I_{15/2}$ and the $^{4}F_{9/2} \rightarrow {}^{4}I_{15/2}$ transitions of Er^{3+}. (b) Excited state level scheme of the activator−sensitizer system comprising Yb^{3+} and Er^{3+} ions in a single nanocrystal. Brown solid, dashed−dotted, and dashed lines indicate absorption, energy transfer (ET), and multiphonon relaxation, respectively. The radiative transitions giving rise to green and red emission are indicated with solid lines. The ground, intermediate, and first excited states are marked with $|0\rangle$, $|1\rangle$, and $|2\rangle$.

the controlled plasmon enhancement of the upconversion PL in $NaYF_4$ nanocrystals doped with Er^{3+} ions together with a reduction of the excited state lifetime.

In this work, we present the first near-field study of rare earth ion doped nanocrystals using a scanning tip. We observe a large tip−sample distance dependent photoluminescence enhancement and discuss sequential two-photon excitation and homoenergy transfer between the ions within the nanocrystal as possible contributions. We complement our discussion by time-resolved PL measurements. In addition, we observe inhomogeneous spatial intensity distributions that are different for the emission wavelengths of Er^{3+}. We attribute this to the interplay between the actual tip shape and the nanocrystal topography becoming particularly relevant in case of large sample structures.

RESULTS AND DISCUSSION

The nanocrystals consisted of a α-$NaYF_4$ crystal matrix doped with Yb^{3+} as a sensitizer and Er^{3+} as an activator. The dopant concentration was 20 mol % for Yb^{3+} and 2 mol % for Er^{3+}, respectively. Due to the preparation procedure (see Methods), the dopant concentration was considered to be homogeneous within the nanocrystal. The excited state level scheme of the activator−sensitizer system showing the two detected transitions in the visible region is presented in Figure 1 together with a schematic of the experimental setup. The tip-enhanced near-field optical microscope combined an inverted oil-immersion

microscope with a shear-force tuning fork AFM instrument. A detailed description of the optical setup is given in Methods.

Figure 2a shows a tip-enhanced near-field image of a nanocrystal probing the $^{4}S_{3/2}$, $^{2}H_{11/2} \rightarrow {}^{4}I_{15/2}$ transition of Er^{3+} together with the simultaneously recorded topography image in Figure 2b. The optical image features two distinct signal contributions: First, there is a narrow circular contribution with nearly uniform intensity and steep edges that dominates the image contrast. Indicated by the dashed lines in Figure 2a,b, this contribution is centered at the position of the nanocrystal as determined from the topography data. The spatial width of the contribution of about 190 nm is clearly below the diffraction limit at the excitation wavelength even considering two-photon absorption ($\sim$$0.51/2^{1/2} \times 980$ nm/NA = 252 nm) and thus demonstrates tip-enhanced near-field interactions. The second, about 400 nm wide signal is the confocal far-field contribution. Its elongated shape is expected. Since the transition dipole moments of the ions are isotropically distributed within the nanocrystal, the confocal image reflects the excitation intensity distribution in the laser focus.[27] Strong focusing is known to lead to two lobes with significant longitudinal field components that are displaced from the center of the focus, rendering a quasi-elliptical intensity distribution. The near-field contribution identified above occurs in one of the longitudinal side lobes, since tip enhancement is strongest for axial field components.[28]
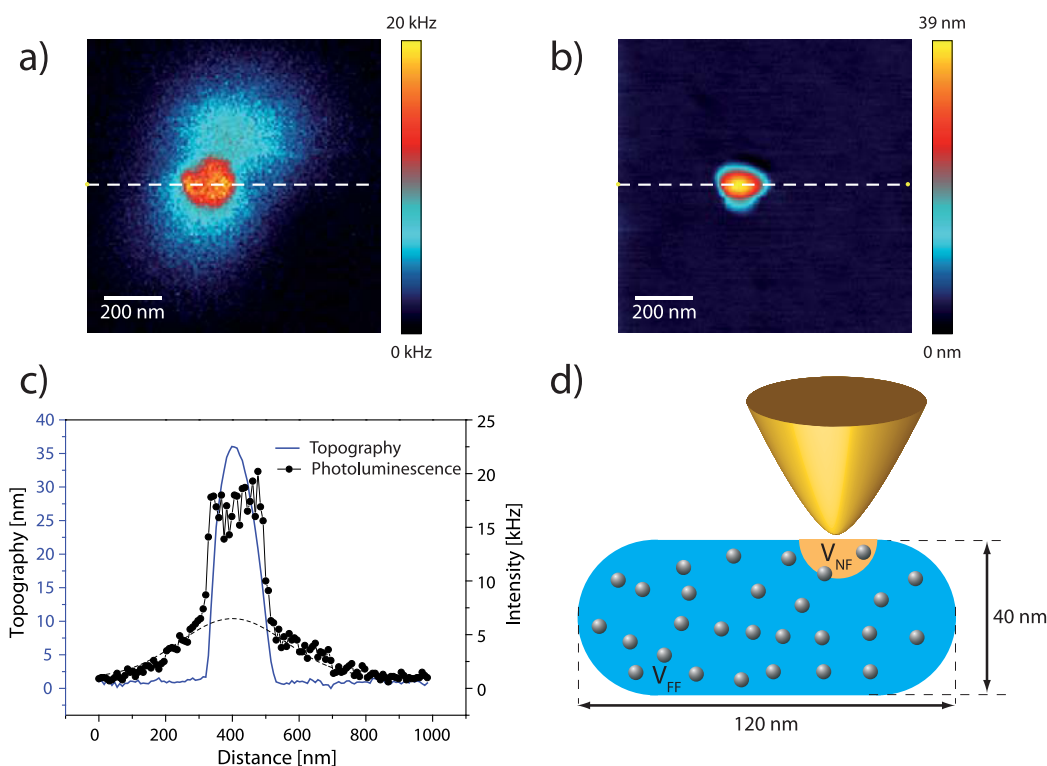
Figure 2. (a) Tip-enhanced upconversion PL image of the green emission at 550 nm upon excitation at 980 nm. In addition to the far-field background, there is a clear subdiffraction enhanced contribution. (b) Topography image taken simultaneously with the image in (a). (c) Topography (blue line) and intensity (black dots) cross sections taken along the white dashed lines in (a) and (b), respectively. The Gaussian fit to the far-field signal is shown as a black dashed line. (d) Schematic of the tip enhancement of the nanocrystal PL together with the nanocrystal dimensions as determined from the topography data in (b). The far-field and near-field volumes are shown in blue and orange, respectively. The gray spheres symbolize the Er^{3+} ions.

To quantify the near-field to far-field image contrast, the signal intensity was extracted along the dashed white line shown in Figure 2a together with a Gaussian fit of the far-field contribution to determine its amplitude. This gave a near-field intensity of about 22 kHz (photon counts per second) and a far-field signal of 7 kHz, respectively, yielding an intensity enhancement of about $I_{NF}/I_{FF} = (29 - 7)/7 \approx 3$. The steep edges and plateaulike pattern in Figure 2a can be understood on the basis of the sketch shown in Figure 2d. Because of the short penetration depth of the locally enhanced field that determines the near-field interaction volume, a further increase of the topographic height did not lead to an increase of the near-field signal.

For the determination of the local signal enhancement factor, the different volumes that contributed to the near-field and far-field signals must be considered.[1,29] Since the nanocrystal size was substantially smaller than the confocal far-field excitation spot, the volume generating the far-field signal corresponds to the nanocrystal volume that could be estimated from the AFM data and the topography profile shown in Figure 2b,c. The AFM data suggest a nanocrystal width of about 200 nm in both lateral directions and a height of 40 nm. The observed shape is of course influenced by the tip geometry. Especially at large nanocrystal

heights, the finite tip diameter and particularly a large opening angle can significantly broaden the observed spatial width. From SEM measurements we know that the tip diameter was initially between 20 and 30 nm, but it could have been increased during the scanning process due to tip wear. In order to estimate the actual nanocrystal volume, we studied the influence of the tip diameter and opening angle on the topography profile by means of simple geometric considerations presented in the Supporting Information. We took into account a broad tip with a large diameter of 60 nm and opening angle of 45° in order to determine a lower limit for the crystal volume. We found that the nanocrystal had at least a width of 120 nm to result in a width of about 200 nm when it was imaged by the tip. The associated volume of 390×10^3 nm^3 was taken as a lower limit for the nanocrystal volume. Because only sharp tips are known to provide a strong electric field enhancement, as observed in Figure 2a, the tip diameter was probably substantially smaller, yielding even larger nanocrystal volumes. A sketch of the experimental configuration including the nanocrystal dimensions is given in Figure 2d, depicting the nanocrystal as an elongated structure. Its endings were approximated by half-spheres in order to simplify the calculations.

According to this sketch, the near-field interaction volume was approximated by a spheric section, with
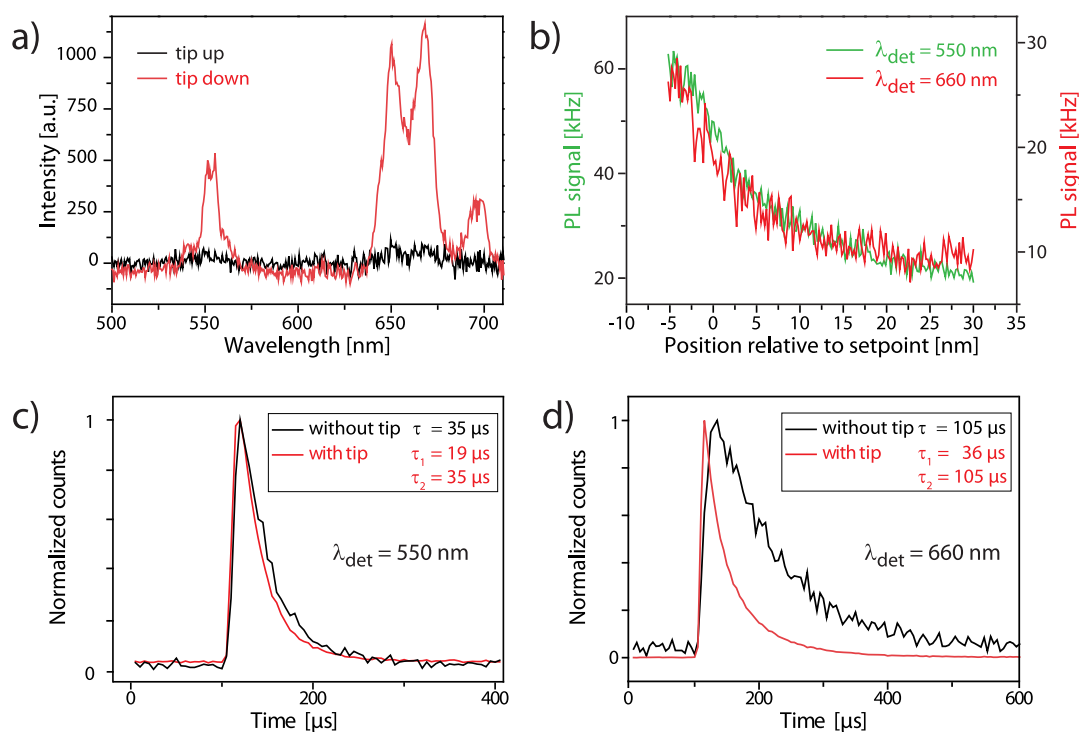
Figure 3. (a) Spectra with retracted and approached tips, respectively. Both emission bands are clearly enhanced. (b) Tip−sample distance dependence of the emission detected at 550 and 660 nm. The continuous signal rise with decreasing tip−sample distance clearly proves the short-range near-field origin of the enhancement. (c, d) Transients for red and green emission detected with and without tip at 550 and 660 nm, respectively. The decay with tip is substantially faster than that without tip. In (b) no signal decrease is observed up to the minimum absolute distance, which would indicate metal-induced quenching. The lifetime reduction is therefore due to radiative rate enhancement.

diameter and height depending on the tip diameter. Assuming a sharp tip with a diameter of 20 nm, it is a half-sphere with a radius of 10 nm corresponding to a sample volume of $V_{NF,min} = [(2/3)\pi] \times 10^3$ nm^3 = 2.1 × 10^3 nm^3. Here, the 10 nm reflects the penetration depth of the near field into the nanocrystal. The near-field interaction volume is associated with an uncertainty coming from the exact tip size. While the lateral extension for a broader tip increases, the penetration depth will probably be less affected due to dielectric screening in the crystal. For a tip with a diameter of 60 nm, the near-field volume was approximated by a spheric section with a radius of 30 nm and a height of 15 nm leading to $V_{NF,max} \approx$ 18 × 10^3 nm^3.

On the basis of these considerations, we obtained a minimum value of $V_{FF}/V_{NF} = (390 \times 10^3)/(18 \times 10^3) \approx$ 22 and a maximum value of $V_{FF}/V_{NF} = (390 \times 10^3)/(2.1 \times 10^3) \approx 185$ for the far-field to near-field volume ratio. These values give lower and upper limits of the volume-normalized enhancement ratio of $((I_{NF}/I_{FF})(V_{FF}/V_{NF}))_{min} = 66$ and $((I_{NF}/I_{FF})(V_{FF}/V_{NF}))_{max} = 555$. Remarkably, even the lower limit is substantially larger than what we typically observe for the PL intensity enhancement in other sample materials such as nanotubes and nanowires using similar types of tips.[5,8] These experiments are usually performed using a radially polarized donut mode, which has a strong electric field

component in the direction of propagation leading to a very efficient enhancement. Considering this, the enhancement observed here, using a Gaussian mode, is even more striking.

We measured similar near-field to far-field intensity ratios for several nanocrystals and tips. For the red emission we observed similar or even larger intensity ratios depending on the tip used, as can be seen in the tip up/down spectra in Figure 3a and in Figure 4. For the tip used in Figure 2a, the lower and upper limitd for the volume normalized near-field to far-field ratios of the red emission detected at 660 nm were 330 and 2775 (data not shown). In the following, we discuss the excitation process involving two sequentially absorbed photons as the possible origin of the observed large intensity enhancement.

We developed a model based on rate equations for a simplified energy level scheme similar to that reported by Esteban et al.,[30] including only the three states of Er^{3+} that are involved in the energy transfer, labeled by $|0\rangle$, $|1\rangle$, and $|2\rangle$ in Figure 1b, and two states of Yb^{3+}. We neglected ground state and excited state absorption of Er^{3+} because of the much higher doping concentration of Yb^{3+} and its about 10 times higher absorption cross section.[31,32] We also neglected back-energy transfer from Er^{3+} to Yb^{3+}. The rate equations were then solved for the steady state and the weak excitation regime (see the Supporting Information).
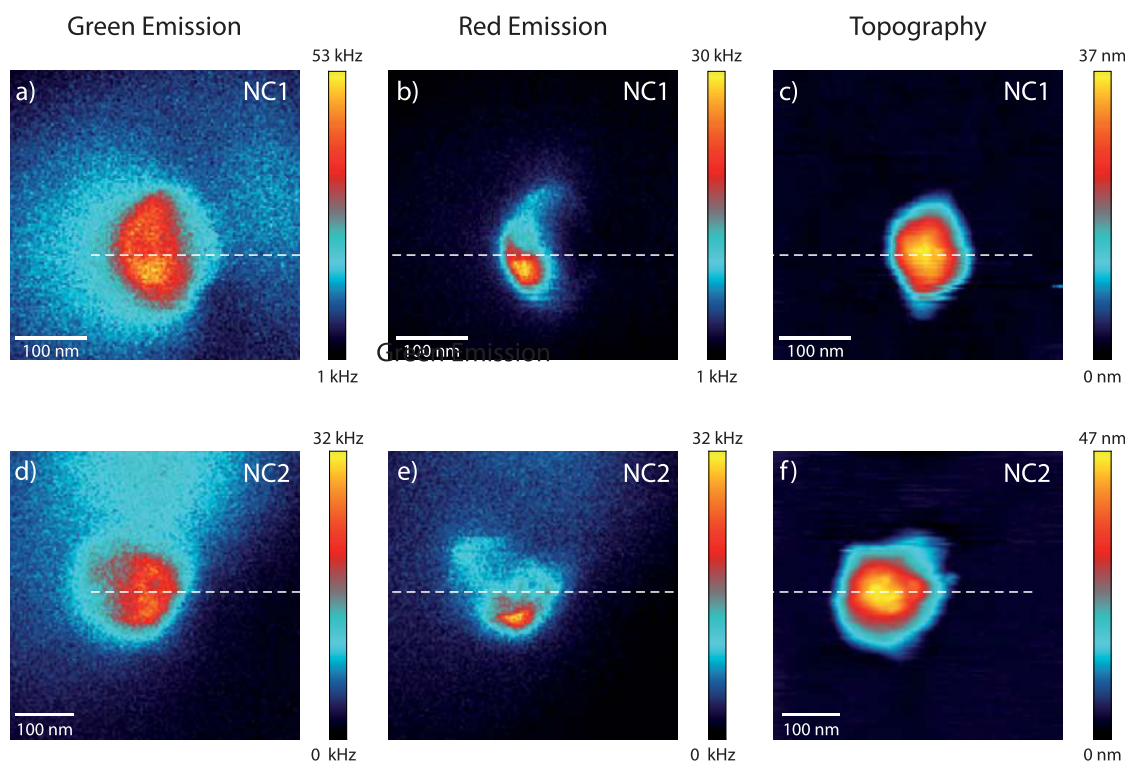
Green Emission — Red Emission — Topography

Figure 4. Simultaneously recorded topography (c, f) and tip-enhanced upconversion photoluminescence images (a, b, d, e) for two different nanocrystals. The red emission shows a stronger image contrast in comparison to the green emission, indicating a stronger signal enhancement for the red wavelength. Both nanocrystals show a nonuniform spatial distribution of the enhanced PL that is localized at the lower nanocrystal edge for the red emission.

The following expression for the signal enhancement for a single sensitizer−activator pair was obtained:

$$\frac{I_{NF}}{I_{FF}} = f_{10}^{\,4}\,\frac{c_{10}}{c_{10}^{\,tip}}\,\frac{\eta_{20}^{\,tip}}{\eta_{20}}\left(\frac{k_{ET}^{\,tip}}{k_{ET}}\right)^2 \frac{(w_{10} + k_{ET}n_{all})^2}{(w_{10}^{\,tip} + k_{ET}n_{all})^2}$$

$$\approx f_{10}^{\,4}\,\frac{c_{10}}{c_{10}^{\,tip}}\,\frac{\eta_{20}^{\,tip}}{\eta_{20}} \tag{1}$$

Here, f_{10} denotes the enhancement factor for the excitation of Yb^{3+}, c_{10} the decay rate of the Er^{3+} intermediate state ($^4I_{11/2}$), w_{10} the decay rate of the Yb^{3+} excited state ($^2F_{5/2}$), k_{ET} the energy transfer rate, and n_{all} the population of all levels of Er^{3+}. η_{20} represents the quantum efficiency of the emitting Er^{3+} state ($^4S_{3/2}$, $^2H_{11/2}$, or $^4F_{9/2}$) and is defined as the ratio between the radiative rate $c_{20}^{\,rad}$ and the sum of all decay rates $\eta_{20} = c_{20}^{\,rad}/(c_{20}^{\,rad} + c_{20}^{\,non\text{-}rad})$. Note that this definition of the quantum efficiency is different from that used for example in ref 33 that measures the ratio between the number of emitted and absorbed photons. As in ref 30, the decay from the emitting to the intermediate state was neglected,: i.e., $c_{21} = 0$. The superscript "tip" indicates the presence of the tip. Assuming that the tip does not influence the energy transfer rate k_{ET} and that the transfer is fast,[30,34] i.e. k_{ET} is large in comparison to w_{10}, the decay of the long-lived excited Yb^{3+} state, the last factor in the first expression of eq 11 can be set to 1. At first glance, the enhancement seems to scale with the fourth power of the absorption enhancement factor f_{10}, as expected for an excitation process involving two photons. However, the excitation enhancement competes with an enhanced depopulation of the $^4I_{11/2}$ level of Er^{3+} and the $^2F_{5/2}$ level of Yb^{3+}. The latter effect is less pronounced and can be neglected because the energy transfer is assumed to be fast and efficient such that most of the Yb^{3+} ions relax via energy transfer and not via radiative means. The former process is accounted for by the factor $((c_{10})/(c_{10}^{\,tip}))$ in eq 11. If there are no nonradiative losses, this expression yields $1/f_{10}^{\,2}$, leading to a quadratic dependence of the signal enhancement on the enhancement factor f_{10}, similar to fluorescence based on one-photon absorption.

Assuming that the Yb^{3+} and Er^{3+} ions do not interact with ions of the same species, eq 11 is also valid for the whole nanocrystal consisting of many ions. Using the obtained approximated expression given in eq 11, we estimated the experimentally observed enhancement. We used approximated values for the quantum efficiency $\eta_{20} \approx 6\%$ (green emission) and $\eta_{10} \approx 30\%$, as described in ref 35, and calculated the ratios $((\eta_{20}^{\,tip})/(\eta_{20}))$ and $((c_{10})/(c_{10}^{\,tip}))$ assuming a typical enhancement factor of about $f_{10} \approx 3$ for the excitation in the near-infrared region and $f_{20} \approx 5$ for the visible region for our standard tips.[5] Inserting these values into eq 11, we obtained a value of $I_{NF}/I_{FF} \approx 240$ for the near-field to far-field intensity ratio. Here, the excitation rate enhancement described by the factor

$f_{10}^4(c_{10}/c_{10}^{tip}) \approx 24$ in eq 11 was more than twice as large as the radiative rate enhancement given by $\eta_{20}^{tip}/\eta_{20} \approx 10$.

The value $I_{NF}/I_{FF} \approx 240$ is in the range of our volume normalized intensity ratio estimated for the green emission above ($66 \leq (I_{NF}/I_{FF})(V_{FF}/V_{NF}) \leq 555$). We note that, in reality, the energy landscape will be far more complex than our simplified scheme depicted in Figure 1b. Nonetheless, this simplified model shows that the upconversion process involving two photons combined with high-field enhancement factors could in principle explain the observed large signal enhancement. However, our model is valid for isolated sensitizer−activator pairs only and neglects coupling among emitters of the same species. In the following, we investigate if energy migration, i.e. energy transfer among Yb^{3+} or Er^{3+} within a single nanocrystal, could play a role.

In fact, the large signal enhancement can also be understood by considering the size and composition of the doped nanocrystals. The high doping concentrations of both types of ions, $c(Yb^{3+}) = 20\%$ and $c(Er^{3+}) = 2\%$, could allow for an efficient energy transfer not only between the Yb^{3+} and Er^{3+} ions (heterotransfer) but also between the Yb^{3+} and Er^{3+} ions themselves (homotransfer), leading to energy migration within the nanocrystal.[36] After locally enhanced excitation in the vicinity of the tip, the electronic energy could be distributed over a larger nanocrystal volume. On the other hand, in the case of efficient transfer, an extended volume could benefit from tip-induced radiative rate enhancement. Energy migration would thus lead to a nonlocal signal contribution, complicating the image contrast formation and the discussion of the signal enhancement.

For Yb^{3+} homotransfer the Förster radius is 2.1 nm; although this was calculated for a different nanocrystal matrix,[37] it is substantially larger than the average ion distance of 0.5 nm (see the Supporting Information) at the present doping concentration. For Er^{3+} homotransfer Förster radii between 1.0 and 1.8 nm are reported, depending on the matrix and transitions,[38−40] comparable to the mean ion distance of 1 nm (see Supporting Information). The Förster radius for the present activator−sensitizer combination is reported to range between 1.5 and 2.0 nm.[37]

With these values we estimated the range of energy migration between the identical ions by calculating the root-mean-square displacment (rmsd) using a 3D random walk model. The rmsd for a diffusive process in three dimensions is given by $(\langle x_2(t) \rangle)^{1/2} = (6Dt)^{1/2}$, where D is the diffusion coefficient depending on the mean ion distance and the energy transfer rate and t the time after which the rmsd is evaluated. The details of the calculations can be found in the Supporting Information. The rmsd depends strongly on the Förster radii and the mean ion distances, since the transfer rate

scales with the sixth power of their ratio. Therefore, we account for an uncertainty for both values of 0.2 nm and estimate lower and upper boundaries for the rmsd.

Assuming a range of 1.9−2.3 nm for the Förster radius and 0.3−0.7 nm for the mean ion separation, an rmsd value ranging from 4 to 50 nm was obtained in the case of energy transfer between Yb^{3+} ions. For Er^{3+} ions, smaller values between 3 and 25 nm were obtained using the given range of Förster radii and an uncertainty of the mean distance of 0.2 nm as for Yb^{3+}. Due to the larger ion separation and the smaller Förster radius, homotransfer between Er^{3+} ions is not as efficient as that between Yb^{3+} ions. Hence, depending on the exact values for the ion distances and Förster radii, the nanocrystal volume affected by energy migration can become comparable to or even larger than the volume probed in the near field. For the lower limits of 4 and 3 nm, respectively, the influence of energy migration will be negligible and the signal enhancement can be calculated according to eq 11. Discussing the upper limit of the migration range, we find the following. After locally enhanced excitation of mainly the Yb^{3+} ions due to their stronger absorption in the vicinity of the tip, the electronic energy could migrate for up to 50 nm, exceeding the near-field interaction range. Since the migration range for the emitting Er^{3+} ions is shorter (25 vs 50 nm), radiative rate enhancement would thus affect not all excited states created by near-field excitation. On the other hand, energy migration between Er^{3+} ions always results in a larger total number of ions benefiting from radiative rate enhancement in comparison to the situation without transfer due to the confocal excitation within the migration range. Our discussion shows the complex interplay between energy transfer processes and the excitation and emission rate enhancement.

We complemented our study by time-resolved measurements, which are shown in Figure 3. The recorded PL transients for both detection energies (Figure 3c,d) show a significantly faster decay in the presence of the tip. In general, this could be due to both tip-induced radiative and nonradiative rate enhancement. To determine which of the two dominates, we recorded tip−sample distance curves for both green and red emission. As can be seen from Figure 3b, the PL intensity increases continuously with increasing slope for decreasing tip−sample distance. Efficient metal-induced quenching that would lead to a decrease of the PL intensity does not occur in the studied tip−sample distance range. This shows that the enhancement of the radiative rate dominates with respect to that of the nonradiative rate. The observed lifetime reduction is therefore mainly due to tip-induced radiative rate enhancement.

In the absence of the tip the transients recorded at both emission wavelengths (Figure 3c,d) can be
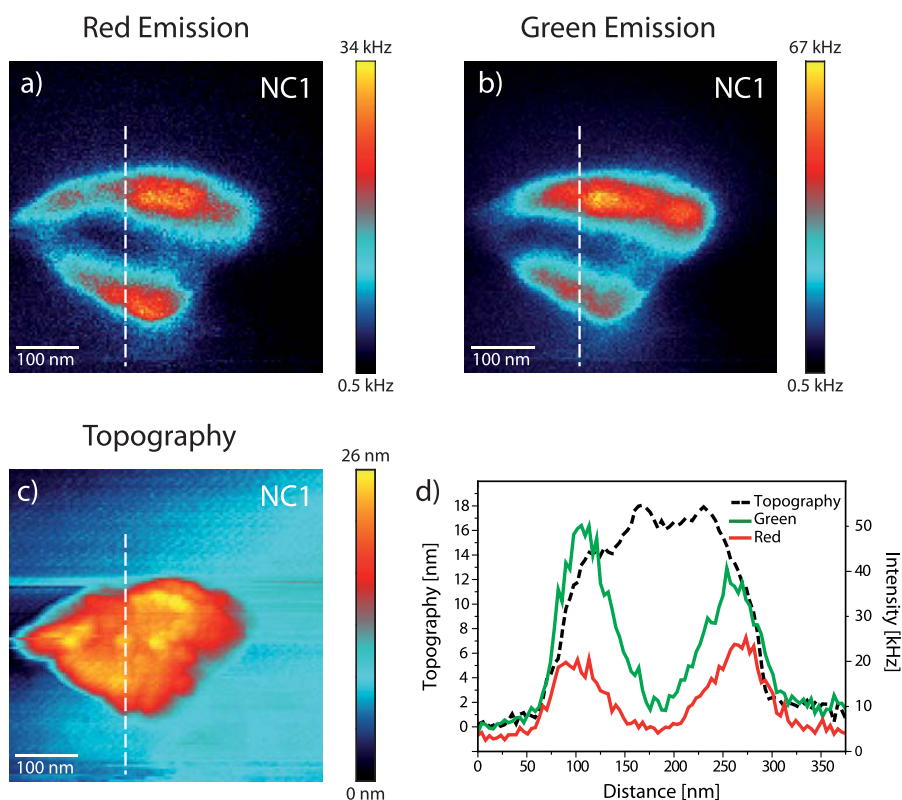
Figure 5. Simultaneously recorded tip-enhanced upconversion photoluminescence images for the (a) $^4F_{9/2} \rightarrow \, ^4I_{15/2}$ and (b) $^4S_{3/2}, \, ^2H_{11/2} \rightarrow \, ^4I_{15/2}$ transitions of nanocrystal NC1 (Figure 4a–c) with another tip. The scan direction is rotated by 55° with respect to Figure 4a–c. The intensity distribution and image contrast are similar for both wavelengths. (c) Simultaneously taken topography image taken simultaneously with those in (a) and (b). Comparing this image with the topography image recorded with the first tip shown in Figure 4c, we conclude that this tip is broader and less defined. (d) PL and topographic cross sections along the white dashed line in (a)–(c). The enhanced PL is the strongest at the nanocrystal edges and nearly disappears in the center. Since ion doping is assumed to be homogeneous, the observed intensity distribution needs to be an artifact resulting from the particular tip shape.

described by monoexponential model functions, yielding lifetimes of 35 and 105 μs for the green and red emission, respectively (see Supporting Information). With the tip the PL decays can be described by biexponential model functions with additional fast decay components of 19 and 36 μs for the green and red emissions, respectively. Transients detected in the presence of the tip only show very small remaining contributions of the decay times detected without tip of 5% for the green emission and 3% for the red emission. This indicates that the local tip-induced radiative rate enhancement indeed leads to a faster relaxation of the emissive states within a larger volume, supporting the idea of homoenergy transfer discussed above.

After a discussion of the upconversion process and the role of homoenergy transfer, we now focus on the influence of the nanocrystal topography on TENOM images. As noted above, the decay length of the enhanced field is limited to about 10–15 nm.[41] While the TENOM signal would thus increase for increasing sample thickness, it is expected to saturate for structures higher than 10–15 nm or in the presence of efficient homoenergy transfer. Indeed, the near-field

upconversion PL image and the cross section shown in Figure 2a,c, respectively, showed this behavior. Plateau-type PL images were also observed for other nanocrystals (Figure 4a,d). For red emission recorded with the same tip, however, the image contrast turned out to be very different (Figure 4b,e). It appeared that, while the whole nanocrystals are seen in the near-field image, additional strong enhancement occurred localized at their lower edges. Since ion doping can be expected to be uniform in lateral direction (see also Methods), we need to conclude that the field enhancement at the tip can be spatially asymmetric. Possible concentration gradients in the radial direction observed for NaGdF$_4$ nanoparticles[42] would not affect the lateral image contrast recorded here. In general, this asymmetry could result from the tip fabrication by electrochemical etching and from tip wear during scanning. Because extended sample structures interact with a larger part of the tip, we expect the resulting influence on the image contrast to be more pronounced than for thin structures that only interact with the foremost part of the tip.

To clarify the influence of the tip on the near-field images further, we studied the image contrast for the

nanocrystal NC1 (Figure 4a−c) using a different tip. Both optical and topographic images are very different, as illustrated in Figure 5. As can be seen from the images in Figure 5a,b and in particular from the cross sections Figure 5d, the intensity is localized at the nanocrystal edges while it disappears in the center. On the basis of the apparent larger topographic width of the nanocrystal and its somewhat irregular shape, we conclude that the tip used was broader and less defined. Given the uniform ion doping and the comparison with Figure 4a−c, the vanishing PL intensity in the center of the nanocrystal must be an artifact. Interestingly, we observed similar enhancement and image contrast for red and green emission in this case. Scanning probe techniques in general are known to be susceptible to imaging artifacts that become particularly relevant for larger sample structures. On the other hand, while the influence of the tip shape on AFM images, for example, can be understood quite well, our data show that for tip-enhanced microscopy it can be far more subtle. In AFM the topography signal can typically described by the convolution between tip shape and sample structure.[43] In tip-enhanced microscopy this does not need to be the case, as can be clearly seen from the spectrally varying contrast in Figure 4. Tip-enhanced near-field optical experiments on higher samples should thus be reproduced and tested with several tips.

In comparison to aperture-based scanning near-field optical microscopy TENOM has two key advantages that are particularly relevant for the study of upconverting nanomaterials. First, metal tips feature superior topographic resolution which is strongly limited for aperture probes.[44,45] Second, aperture probes provide only low throughput due to the cutoff of propagating waveguide modes, precluding the use of the high excitation intensities needed for two-photon processes.[46]

CONCLUSIONS

In summary, we investigated the enhancement of upconversion PL of rare earth ion doped nanocrystals using a scanning metal tip. Tip-enhanced near-field optical (TENOM) images of single nanocrystals showed strong PL amplification and clear subdiffraction spatial resolution as a result of tip-enhanced optical fields. Using a simplified energy level scheme, we derived a quantitative model for the enhancement mechanism and the resulting enhancement factors that are in general agreement with the experimentally observed near-field to far-field ratios. According to this model, the effect of excitation rate enhancement, although expected to be highly efficient in case of an excitation process involving two photons, can cancel out due to the competing depopulation of the intermediate states. The contribution of radiative rate enhancement, on the other hand, is clearly confirmed using time-resolved PL spectroscopy and tip−sample distance curves. Considering the high ion doping levels in the nanocrystals, we suggested an additional nonlocal contribution to the tip-enhanced signal caused by efficient nonradiative homoenergy transfer between the ions in the nanocrystals. Near-field images recorded using different tips showed a strong influence of the tip shape that could lead to imaging artifacts. In contrast to other scanning probe techniques such as AFM, in TENOM the influence of the tip is more subtle and cannot be described directly using its geometrical parameters. Our studies clearly show that TENOM can be successfully applied to single nanocrystals and indicate the potential of the technique for the characterization of more complex upconverting functional materials on the nanoscale.

METHODS

Sample Preparation. α-NaYF$_4$ nanocrystals were synthesized following the procedure described previously in ref 47. During the doping process Y^{3+} ions were randomly replaced by equi-charged Yb^{3+} and Er^{3+} ions at levels of 20% and 2%, respectively. XRD measurements of the doped nanocrystals reveal a purely cubic crystal phase without detectable structural impurities. We thus assume rather homogeneous codoping within the whole nanocrystals. We note that for differently doped NaGdF$_4$ nanoparticles nonstatistical dopant distributions in the radial direction were observed using synchrotron radiation.[42] In the case of Y and Tb codoping a subtle concentration gradient in the radial direction was observed with Gd^{3+} more concentrated toward the center and Y^{3+} more concentrated toward the surface. Steeper radial concentration gradients were detected for Nd^{3+} and Tb^{3+} doping. While radial concentration gradients cannot be excluded for the present nanocrystals as well, we would expect no lateral gradients that could affect the image contrast in a scanning probe measurement across the nanocrystal surface. The nanocrystals dispersed in chloroform were spin-coated onto a glass substrate for the optical and topographic measurements.

Microscope Setup. The optical setup combined an inverted confocal oil immersion microscope with a tuning fork shear-force distance control that enabled scanning of a sharp gold tip centered in the laser focus in close proximity to the sample. A scheme of the setup is shown in Figure 1a. The nanocrystals were excited with a Gaussian laser beam at 980 nm focused by a high NA objective (NA = 1.49) onto the nanocrystals. The excitation power used in the experiment was about 0.3 mW, taking into account the transmission of the microscope objective. This corresponds to an excitation intensity of 40 kW/cm^2 within the focus. For image acquisition the sample was raster scanned while keeping tip and focus position fixed. The detection path was split into two channels in order to record two emission bands simultaneously. The two emission bands belong to the $^4S_{3/2}, ^2H_{11/2} \rightarrow ^4I_{15/2}$ and the $^4F_{9/2} \rightarrow ^4I_{15/2}$ transition of Er^{3+} (see Figure 1b) and were detected using two APDs after band-pass filtering centered at 550 ± 25 nm for the green emission and at 660 ± 15 nm for the red emission, respectively. No additional detection pinhole was used. Hence, the spatial resolution of the confocal experiments was given by diffraction at the excitation wavelength $\Delta x \approx (0.51/2^{1/2}) \times (980 \text{ nm}/NA) = 252 \text{ nm}$. For time-resolved measurements we used a multiscaler

REFERENCES AND NOTES

1. Mauser, N.; Hartschuh, A. Tip-Enhanced Near-Field Optical Microscopy. *Chem. Soc. Rev.* **2014**, *43*, 1248–1262.
2. Bharadwaj, P.; Deutsch, B.; Novotny, L. Optical Antennas. *Adv. Opt. Photon.* **2009**, *1*, 438–483.
3. Anderson, N.; Anger, P.; Hartschuh, A.; Novotny, L. Subsurface Raman Imaging with Nanoscale Resolution. *Nano Lett.* **2006**, *6*, 744.
4. Zhang, D.; Heinemeyer, U.; Stanciu, C.; Sackrow, M.; Braun, K.; Hennemann, L. E.; Wang, X.; Scholz, R.; Schreiber, F.; Meixner, A. J. Nanoscale Spectroscopic Imaging of Organic Semiconductor Films by Plasmon-Polariton Coupling. *Phys. Rev. Lett.* **2010**, *104*, 056601.
5. Böhmler, M.; Hartmann, N.; Georgi, C.; Hennrich, F.; Hersam, M. C.; Hartschuh, A. Enhancing and Redirecting Carbon Nanotube Photoluminescence by an Optical Antenna. *Opt. Express* **2010**, *18*, 16443–16451.
6. Rauhut, N.; Engel, M.; Steiner, M.; Krupke, R.; Avouris, P.; Hartschuh, A. Antenna-Enhanced Photocurrent Microscopy on Single-Walled Carbon Nanotubes at 30nm Resolution. *ACS Nano* **2012**, *6*, 6416–6421.
7. Böhmler, M.; Wang, Z.; Myalitsin, A.; Mews, A.; Hartschuh, A. Optical Imaging of CdSe Nanowires with Nanoscale Resolution. *Angew. Chem., Int. Ed.* **2011**, *50*, 11536.
8. Böhmler, M.; Hartschuh, A. Tip-Enhanced Near-Field Optical Microscopy of Single Quasi-1D Nanostructures. *ChemPhysChem* **2012**, *13*, 927.
9. Bao, W.; Melli, M.; Caselli, N.; Riboli, F.; Wiersma, D. S.; Staffaroni, M.; Choo, H.; Olgetree, D. F.; Aloni, S.; Bokor, J.; et al. Mapping Local Charge Recombination Heterogeneity by Multidimensional Nanospectroscopic Imaging. *Science* **2012**, *338*, 1317–1321.
10. Steidtner, J.; Pettinger, B. Tip-enhanced Raman Spectroscopy and Microscopy on Single Dye Molecules with 15nm Resolution. *Phys. Rev. Lett.* **2008**, *100*, 236101.
11. Taminiau, T. H.; Stefani, F. D.; Segerink, F. B.; van Hulst, N. F. Optical Antennas Direct Single-Molecule Emission. *Nat. Photonics* **2008**, *2*, 234–237.
12. Bailo, E.; Deckert, V. Tip-Enhanced Raman Spectroscopy of Single RNA Strands: Towards a Novel Direct-Sequencing Method. *Angew. Chem. Int. Ed.* **2008**, *47*, 1658–1661.
13. Stadler, J.; Schmid, T.; Zenobi, R. Nanoscale Chemical Imaging of Single-Layer Graphene. *ACS Nano* **2011**, *5*, 8442–8448.
14. Su, W.; Roy, D. Visualizing Graphene Edges Using Tip-Enhanced Raman Spectroscopy. *J. Vac. Sci. Technol. B* **2013**, *31*, 041808.
15. Sánchez, E. J.; Novotny, L.; Xie, X. S. Near-Field Fluorescence Microscopy Based on Two-Photon Excitation with Metal Tips. *Phys. Rev. Lett.* **1999**, *82*, 4014–4017.
16. Zhang, R.; Zhang, Y.; Dong, Z. C.; Jiang, S.; Zhang, C.; Chen, L. G.; Zhang, L.; Liao, Y.; Aizpurua, J.; Luo, Y. e. a. Chemical Mapping of a Single Molecule by Plasmon-Enhanced Raman Scattering. *Nature* **2013**, *498*, 82–86.
17. Georgi, C.; Böhmler, M.; Qian, H.; Novotny, L.; Hartschuh, A. Probing Exciton Propagation and Quenching in Carbon Nanotubes with Near-Field Optical Microscopy. *Phys. Stat. Sol. B* **2009**, *246*, 2683.
18. Kumar, R.; Nyk, M.; Ohulchanskyy, T. Y.; Flask, C. A.; Prasad, P. N. Combined Optical and MR Bioimaging Using Rare Earth Ion Doped NaYF$_4$ Nanocrystals. *Adv. Funct. Mater.* **2009**, *19*, 853–859.
19. Liu, Q.; Sun, Y.; Li, C.; Zhou, J.; Li, C.; Yang, T.; Zhang, X.; Yi, T.; Wu, D.; Li, F. 18F-Labeled Magnetic-Upconversion Nanophosphors *via* Rare-Earth Cation-Assisted Ligand Assembly. *ACS Nano* **2011**, *5*, 3146–3157.
20. Sark, W. G. v.; Wild, J. d.; Rath, J. K.; Meijerink, A.; Schropp, R. E. Upconversion in Solar Cells. *Nanoscale Res. Lett.* **2013**, *8*, 1–10.
21. Kassab, L. R. P.; de Araújo, C. B.; Kobayashi, R.; de Almeida Pinto, R.; da Silva, D. M. Influence of Silver Nanoparticles in the Luminescence Efficiency of Pr^{3+}-Doped Tellurite Glasses. *J. Appl. Phys.* **2007**, *102*, 103515.
22. Kassab, L. R. P.; da Silva, S. D.; de Almeida Pinto, R.; de Araújo, C. B. Photoluminescence Enhancement by Gold Nanoparticles in Eu^{3+} Doped GeO$_2$-Bi$_2$O$_3$ Glasses. *Appl. Phys. Lett.* **2009**, *94*, 101912.
23. Rai, V.; Menezes, L.; de Araújo, C.; Kassab, L.; da Silva, D.; Kobayashi, R. Surface-Plasmon-Enhanced Frequency Upconversion in Pr^{3+} Doped Tellurium-Oxide Glasses Containing Silver Nanoparticles. *J. Appl. Phys.* **2008**, *103*, 093526.
24. Sun, Q. C.; Mundoor, H.; Ribot, J. C.; Singh, V.; Smalyukh, I. I.; Nagpal, P. Plasmon-Enhanced Energy Transfer for Improved Upconversion of Infrared Radiation in Doped-Lanthanide Nanocrystals. *Nano Lett.* **2014**, *14*, 101–106.
25. Lu, D.; Cho, S. K.; Ahn, S.; Brun, L.; Summers, C. J.; Park, W. Plasmon Enhancement Mechanism for the Upconversion Processes in NaYF$_4$:Yb^{3+}, Er^{3+} Nanoparticles: Maxwell versus Förster. *ACS Nano* **2014**, 1–2.
26. Schietinger, S.; Aichele, T.; Wang, H.-Q.; Nann, T.; Benson, O. Plasmon-Enhanced Upconversion in Single NaYF$_4$:Yb^{3+}/ Er^{3+} Codoped Nanocrystals. *Nano Lett.* **2010**, *10*, 134–138.
27. Hartmann, N.; Piatkowski, D.; Ciesielski, R.; Mackowski, S.; Hartschuh, A. Radiation Channels Close to a Plasmonic Nanowire Visualized by Back Focal Plane Imaging. *ACS Nano* **2013**, *7*, 10257–10262.
28. Novotny, L.; Sánchez, E. J.; Xie, X. S. Near-field Optical Imaging Using Metal Tips by Higher-Order Hermite-Gaussian Beams. *Ultramicroscopy* **1998**, *71*, 21.
29. Roy, D.; Wang, C.; Williams, J. Novel methodology for estimating the enhancement factor for tip-enhanced Raman spectroscopy. *J. Appl. Phys.* **2009**, *105*, 013530.
30. Esteban, R.; Laroche, M.; Greffet, J. J. Influence of Metallic Nanoparticles on Upconversion Processes. *J. Appl. Phys.* **2009**, *105*, 033107.
31. Strohhöfer, C.; Polman, A. Relationship Between Gain and Yb^{3+} Concentration in Er^{3+}- Yb^{3+} Doped Waveguide Amplifiers. *J. Appl. Phys.* **2001**, *90*, 4314–4320.
32. Piatkowski, D.; Mackowski, S. Excited state absorption in glasses activated with rare earth ions: Experiment and modeling. *Optical Mater.* **2012**, *34*, 2055–2060.
33. Boyer, J. C.; van Veggel, F. C. J. M. Absolute quantum yield measurements of colloidal NaYF$_4$: Er^{3+}, Yb^{3+} upconverting nanoparticles. *Nanoscale* **2010**, *2*, 1417.
34. Blum, C.; Zijlstra, N.; Lagendijk, A.; Wubs, M.; Mosk, A. P.; Subramaniam, V.; Vos, W. L. Nanophotonic Control of the Förster Resonance Energy Transfer Efficiency. *Phys. Rev. Lett.* **2012**, *109*, 203601.
35. We estimated the quantum efficiency η_{20} of the green emission dividing the experimentally measured lifetime τ_{exp}= 35 μs by a theoretical value of τ_{calc} = 550 μs

calculated by the Judd−Ofelt theory[48] considering only radiative decay. η_{10} is estimated in the same way using a value for the experimental lifetime of $\tau_{exp} = 3000\,\mu s$ for the $^4I_{11/2}$ state taken from refs 49 and 50 and $\tau_{calc} = 9000\,\mu s$.

36. Auzel, F. Upconversion and Anti-Stokes Processes with F and D Ions in Solids. *Chem. Rev.* **2004**, *104*, 139–173.

37. Ward, J. M.; O'Shea, D. G.; Shortt, B. J.; Chormaic, S. N. Optical Bistability in Er-Yb Codoped Phosphate Glass Microspheres at Room Temperature. *J. Appl. Phys.* **2007**, *102*, 023104.

38. Yan, Y.; Faber, A. J.; de Waal, H. Luminescence Quenching by OH Groups in Highly Er-Doped Phosphate Glasses. *J. Non-Cryst. Solids* **1995**, *181*, 283–290.

39. Miguel, R.; Al-Saleh, A.; Azkargorta, M.; Morea, J.; Gonzalo, R.; Arriandiaga, J.; Fernandez, M. A.; Balda, J. Spectroscopic Properties of Er³⁺-Doped Fluorotellurite Glasses. *Opt. Mater.* **2013**, *35*, 2039–2044.

40. Jaba, N.; BenMansour, H.; Kanoun, A.; Brenier, A.; Champagnon, B. Spectral Broadening and Luminescence Quenching of 1.53 μm Emission in Er³⁺-Doped Zinc Tellurite Glass. *J. Lumin.* **2009**, *129*, 270–276.

41. Anderson, M. S.; Gaimari, S. D. Raman-Atomic Force Microscopy of the Ommatidial Surfaces of Dipteran Compound Eyes. *J. Struct. Biol.* **2003**, *142*, 364–368.

42. Dong, C.; Pichaandi, J.; Regier, T.; van Veggel, F. C. J. M. Nonstatistical Dopant Distribution of Ln³⁺-Doped NaGdF₄ Nanoparticles. *J. Phys. Chem. C* **2011**, *115*, 15950.

43. Canet-Ferrer, J.; Coronado, E.; Forment-Aliaga, A.; Pinilla-Cienfuegos, E. Correction of the tip convolution effects in the imaging of nanostructures studied through scanning force microscopy. *Nanotechnology* **2014**, *25*, 395703.

44. Veerman, J. A.; Otter, A. M.; Kuipers, L.; van Hulst, N. F. High Definition Aperture Probes for Near-Field Optical Microscopy Fabricated by Focused Ion Beam Milling. *Appl. Phys. Lett.* **1998**, *72*, 3115.

45. Frey, H. G.; Keilmann, F.; Kriele, A.; Guckenberger, R. Enhancing the Resolution of Scanning Near-Field Optical Microscopy by a Metal Tip grown on an Aperture Probe. *Appl. Phys. Lett.* **2002**, *81*, 530.

46. Novotny, L., Hecht, B. *Principles of Nano-Optics*; Cambridge University Press: Cambridge, U.K., 2006.

47. Nyk, M.; Kumar, R.; Ohulchanskyy, T. Y.; Bergey, E. J.; Prasad, P. N. High Contrast *in Vitro* and *in Vivo* Photoluminescence Bioimaging Using Near Infrared to Near Infrared Up-Conversion in Tm³⁺ and Yb³⁺ Doped Fluoride Nanophosphors. *Nano Lett.* **2008**, *8*, 3834–3838.

48. Ofelt, G. S. Intensities of Crystal Spectra of Rare-Earth Ions. *J. Chem. Phys.* **1962**, *37*, 511.

49. Judd, B. R. Optical Absorption Intensities of Rare-Earth Ions. *Phys. Rev.* **1962**, *127*, 750.

50. Pokhrel, M.; Kumar, G. A.; Sardar, D. K. Highly efficient NIR to NIR and VIS upconversion in Er³⁺ and Yb³⁺ doped in M₂O₂S (M = Gd, La, Y). *J. Mater. Chem. A* **2013**, *1*, 11595.